CHALMERS
UNIVERSITY OF TECHNOLOGY

The effect of additive manufacturing on the initial High temperature oxidation properties of RE-containing FeCrAl alloys

Corrosion Science 188 (2021) 109553

Contents lists available at ScienceDirect

Corrosion Science

journal homepage: www.elsevier.com/locate/corsci

The effect of additive manufacturing on the initial High temperature oxidation properties of RE-containing FeCrAl alloys

K. Ozgur Gunduz [a,b], Alberto Visibile [a], Mohammad Sattari [c], Irina Fedorova [c], Saud Saleem [d], Krystyna Stiller [c], Mats Halvarsson [c], Jan Froitzheim [a,*]

[a] Chalmers University of Technology, Department of Chemistry and Chemical Engineering, Division of Energy and Materials, SE-412 96, Gothenburg, Sweden
[b] Gebze Technical University, Department of Materials Science and Engineering, 41400, Gebze, Kocaeli, Turkey
[c] Chalmers University of Technology, Department of Physics, Division of Microstructure Physics, SE-412 96, Gothenburg, Sweden
[d] Kanthal AB, Sörkvarnsvägen 3, SE-734 27, Hallstahammar, Sweden

ARTICLE INFO

Keywords:
Additive manufacturing
3D printing
High temperature oxidation
Corrosion
FeCrAl alloys
Microstructure

ABSTRACT

The effect of additive manufacturing on the high temperature oxidation properties of FeCrAl materials was investigated. For this purpose, additively manufactured Kanthal AM100 cut parallel and perpendicular to the building direction and hot-rolled Kanthal AF as a reference were exposed to air at 900 and 1100 °C for 168 h. AM100 performed slightly better than AF in terms of mass gain. Nevertheless, an oxide scale with local differences in thickness formed on AM100 due to the bimodal grain structure of the underlying metal, which was composed of coarse-grained cuboidal repeating units (100 μm wide), separated by fine-grained rims.

1. Introduction

Fe-Cr-Al alloys are known for their excellent oxidation resistance and are utilized in many high temperature applications, such as heating elements for furnaces, construction materials for concentrated solar power systems, catalyst support for automobiles, and cladding material against fuel accidents in nuclear power plants [1–4].

The excellent oxidation resistance of Fe-Cr-Al alloys is related to the formation of a slow-growing protective α-alumina (α-Al_2O_3) oxide scale. The oxidation process of alumina-forming alloys starts at low temperatures (T < 900 °C) with the formation of poorly protective outward-growing transient Al_2O_3 phases, such as δ-Al_2O_3, θ-Al_2O_3, and γ-Al_2O_3. With time, these transient phases might convert to the stable α-Al_2O_3 phase, depending on the temperature and oxidizing media [5–10]. The formation of α-Al_2O_3 dominates at higher temperatures (T > 1000 °C) even in the very early stages of oxidation [11]. The addition of Cr as a third element facilitates the formation of α-Al_2O_3 with a much lower content of Al in Fe-Cr-Al or Ni-Cr-Al alloys. This is accomplished by the formation of a thin Cr_2O_3 layer in the transition stage, which provides easy nucleation sites for α-Al_2O_3 since both phases crystallize in the corundum structure [12–14].

Alumina-forming alloys are usually prone to spallation, especially under cyclic oxidation conditions. Therefore, they are alloyed with very small amounts (in the ppm range) of reactive elements (RE), such as Y, Hf, Zr, Ce, or their oxides, such as Y_2O_3, or ZrO_2. The addition of reactive elements improves scale adhesion and slows down the growth rate of the oxide scale [6,15–18]. Oxides of reactive elements have been found to enhance the creep strength of Fe-Cr-Al alloys through a dispersion-hardening mechanism [19,20]. This is important since the Al content of this alloy group is limited to 5 wt. %, as any further addition of Al decreases alloy ductility, which would cause severe metallurgical processing problems with conventional fabrication methods, such as rolling [21,22].

Components traditionally made of Fe-Cr-Al alloys are manufactured with casting and plastic deformation techniques, such as hot rolling and powder metallurgy (ODS steels). However, manufacturing complex geometries for various applications with these processes is complicated and might require extra processing, such as machining or welding [23,24].

Additive manufacturing (AM) is a relatively new production method where 3D objects are created by adding layer upon layer of a material according to a 3D computer design. The advantage of this process is that even very complex-shaped components can be produced without the limitations of conventional manufacturing methods [23,24]. The most common AM process for metals is powder bed fusion (PBF), where subsequent metal powder layers are selectively melted or sintered into

* Corresponding author.
E-mail address: jan.froitzheim@chalmers.se (J. Froitzheim).

https://doi.org/10.1016/j.corsci.2021.109553
Received 23 November 2020; Received in revised form 10 May 2021; Accepted 12 May 2021
Available online 13 May 2021

the desired shape. This is accomplished with a laser source, such as either (laser beam melting, (LBM)) or (direct metal laser sintering (DMLS)), or with an electron beam as the heat source (electron beam melting (EBM)). Compared to EBM, LBM requires less expensive equipment, provides a better surface finish (R_a: 4−11 μm vs R_a: 25−35 μm), easy removal of loose powder, and a faster building rate [25].

However, the additive manufacturing of metallic alloys results in unusual microstructures that are highly anisotropic, with respect to parallel and perpendicular to the building direction (BD) [26–28]. Depending on the AM parameters and alloy composition, pore formation and layer delamination occur during the solidification process [29,30]. A study by Shi et al. [31] has shown that a Zr-containing ODS Fe-Cr-Al alloy produced with AM had an ultimate tensile strength (UTS) value of 370 MPa and a total elongation (TE) value of 3.6 % parallel to the BD. This alloy also had a UTS value of 410 MPa and a TE value of 14 % perpendicular to the BD. In addition to mechanical properties, the oxidation properties of AM-produced Al_2O_3 and Cr_2O_3-forming materials are also extremely important as these alloys are designed to be used at elevated temperatures.

The high temperature oxidation properties of additively manufactured materials are a newly emerging field of research. Hence, a limited number of studies have been published on the subject. To the best of the authors knowledge, there is no study on the effects of additively manufactured microstructures on the high-temperature oxidation of FeCrAl alloys containing RE.

We report on the initial high temperature oxidation properties of an LBM-produced RE-modified Fe-Cr-Al alloy (Kanthal AM100) exposed at 900 °C and 1100 °C. These exposure temperatures were chosen because Fe-Cr-Al alloys typically operate between 900 °C and 1200 °C. A relatively short exposure duration of 168 h was chosen to observe and determine the effect of the microstructure in relation to the production method of Fe-Cr-Al alloys. We compared the Kanthal AM100 alloy with the wrought RE-containing Fe-Cr-Al alloy Kanthal AF, to investigate the effect of microstructure on oxidation properties.

2. Experimental

2.1. Materials

Additively manufactured Kanthal AM100 and wrought Kanthal AF (hereinafter referred to as AM100 and AF, respectively) alloys were provided by Kanthal. The compositions of the alloys are given in Table 1. C, O, and N contents were determined with combustion according to ASTM E1019. Mg content was determined with ICP-OES, and the rest of the elements were measured with XRF according to ASTM E572.

The AF material was produced with hot rolling and was provided as metal strips with the dimensions of 1 m x 10 mm x 2 mm. The AM100 material was produced with LBM in the form of metal cubes with the dimensions of 10 mm x 10 mm x 10 mm. The LBM process was performed under a controlled argon atmosphere to minimize oxidation during the melting and solidification cycles. A bidirectional laser beam scanning strategy was used so that subsequent layers had a 90° rotation with respect to each other. The following parameters were used for the AM process: Energy density: 2–2.5 J/mm^2, hatch distance (one scanning step): 78 μm, and laser spot diameter: 50 μm.

2.2. Preparation and characterization of alloys

Prior to the oxidation experiments, the AM100 alloy was heat treated at 850 °C for 15 min to relieve the residual stresses formed during the LBM process. The AM100 cubes were sectioned with a Struers Minitom low speed saw to obtain samples with the desired dimensions for furnace exposure, 10 mm× 10 mm × 1 mm. Samples were sectioned parallel and perpendicular to the BD to account for the inhomogeneity of the microstructure in different directions. Samples sectioned parallel and perpendicular to the BD will hereinafter be referred to as AM100-Y and AM100-Z, respectively. After cutting, the two large faces were gradually polished with the final step being diamond paste of 1 μm, while the edges (10 × 1 mm) of the samples were ground with SiC emery papers, ending with 4000 grit. After polishing, each sample was rinsed with deionized water and then placed in an ultrasonic bath of acetone and ethanol twice for 10 min each time. One sample of each type was electrolytically etched in a 0.1 g ml^{-1} oxalic acid solution to reveal the microstructure in the as-printed stress-relieved condition. Only polished samples (not etched) were exposed. A ZEISS Leo Ultra 55 scanning electron microscope (SEM) equipped with a Nordlys electron backscatter diffraction (EBSD) detector was used to determine the crystallographic texture of some of the polished samples.

2.3. Oxidation tests

A Mettler Toledo XP6 microbalance with 1 μg resolution was used to weigh the samples before and after the exposures. Isothermal exposures were performed in tube furnaces at 900 °C and 1100 °C under 0.7 m/min flow velocity for 168 h in filtered laboratory air. Temperature profiling of the furnaces were accomplished by inserting an external S-Type thermocouple in 2 cm steps from downstream to upstream of the furnace. The thermocouple was equilibrated for an hour between each step to ensure that it showed the correct temperature. The samples were placed in the hottest zone where the temperature deviated by 3 °C within 5 cm. Each sample type was exposed at least twice to check for repeatability and to minimize statistical errors. The samples were weighed again after the exposures to determine their mass gain.

2.4. Post exposure characterizations

A Siemens D5000 diffractometer (Cu K_α radiation) was employed for grazing incidence X-ray diffraction (GI-XRD). A grazing incidence angle of 0.5−2° was used, and a 2θ range of 20°-90° was measured with a step size of 0.05°. SEM analyses were performed with an FEI ESEM Quanta 200 FEG equipped with an Oxford Instruments X-MAX 80 energy dispersive X-ray spectroscopy (EDX) detector and a ZEISS Leo Ultra 55 SEM. SEM-EDX analysis were performed with 20 kV accelerating voltage at a working distance of 10 mm, aperture 4, and a process time of 3, which corresponds to 40 % dead time. It should be mentioned that SEM-EDX analysis was only performed on polished samples prior to exposures and as-oxidized (plan view) and BIB-milled cross-sections. Site-specific cross-sections and lift-outs were made using a FEI Versa 3D focused ion beam/scanning electron microscope (FIB/SEM) equipped with an Oxford Instruments OmniProbe 100 micromanipulator system. Analytical scanning transmission electron microscopy (STEM/EDX) analyses were carried out with an FEI Titan 80–300 TEM/STEM probe-corrected microscope operated at 300 keV and equipped with an Oxford Instruments INCA X-sight EDX system.

Table 1
Chemical composition of Kanthal AF and Kanthal AM100.

Element (wt.%)	Fe	Cr	Al	Si	C	N	O	Mg	Minor elements (<1000 ppm)
Kanthal AF	Bal.	21.3	5.5	0.3	0.01	0.02	<0.002*	<0.009	Ti,Y,Zr
Kanthal AM100	Bal.	21.6	5.3	0.3	0.02	0.03	0.04	<0.001	Ti,Y,Zr

* Typical value.

3. Results and discussion

3.1. Investigation of alloys prior to exposure

Results from the analyses of both AF and AM100 materials in unexposed conditions are presented in Figs. 1 and 2. Fig. 1 shows micrographs from the SEM of the polished and etched AF, AM100-Z, and AM100-Y samples. Fig. 2 shows the EDX analysis performed on AM100-Z and the EBSD analysis performed on AM100-Z and AM100-Y. As shown in Fig. 1c and f, AF had an isotropic microstructure consisting of equiaxed grains around 10−20 μm in size with well-dispersed RE particles. A previous study on AF has shown that most of the RE precipitates in AF vary in composition; some of them are rich in Zr, while others are rich in Y [32].

The materials produced with the AM process have a unique and unprecedented microstructure. The microstructural investigation of AM100-Y (Fig. 1b and e) revealed that the material consisted of repeating columns parallel to the BD, while the AM100-Z sample had a square-shaped pattern perpendicular to the BD (Fig. 1a, d). The columns were approximately 100 μm wide, which matched well the size of the squares, indicating that they represented the top view of the columns. Repeating narrow rims, approximately 5 μm in size, were visible between the columns and squares. These narrow rims consisted of submicron-sized grains (Fig. 1d and e). In addition, melt pool lines, characteristic of additively manufactured materials, were also visible parallel to the BD on the AM100-Y (Fig. 1e) sample. It should be noted that the features on the rims are etching pits as those regions were more defective and more prone to react with the etchant. According to the inverse pole figure (IPF) maps obtained with the EBSD analysis (Fig. 2b and c), most of the narrow rims were oriented in the <001> direction, while the columns were mostly oriented in the <111> direction, although some of them were also oriented in the <101> direction. Interestingly, the orientation of the columnar grains and the narrow rims was not interrupted by the melt pool lines that passed through them. This behavior is explained in the literature as the epitaxial growth of newly deposited material on previously solidified grains on columns and narrow rims, which maintains the same orientation [33,34]. The IPF maps (Fig. 2b and c) show that some of the squares were almost single crystal, while others were composed of multiple grains. The peculiar microstructure of the square-shaped columns was formed because of the laser beam scanning strategy and processing parameters. As the beam angle changed 90° sequentially in each scan, it formed a 3D array of cuboidal columns that were separated by narrow rims acting as boundaries between each square and/or column. This assertion is further supported by the hatch distance and beam size used in this study, 78 and 50 μm, respectively, which matched perfectly with the sizes of the squares and columns. A study by Pham et al. [35] has shown that employing a similar scanning strategy to 316 L resulted in the same type of microstructure.

It is also believed that the presence of small grains on the narrow rims is related to the temperature of the melt and heat transfer during solidification, which is a function of laser energy, scanning speed, beam size, and hatch distance. During each scan, the narrow rims were less heated by the laser than the columns, resulting in a lower melt temperature [36,37]. As a result of low melt temperature combined with the fast cooling, the narrow rims were subjected to a high thermal gradient that mitigated the growth of nucleated grains during the solidification process. This difference in thermal gradient not only affected the morphology but also the orientation of grains, as shown in the IPF maps (Fig. 2b and c), since the narrow rims were oriented differently than the columns and squares.

The SEM analysis of RE particles in AF and AM material revealed that these particles were bigger, approximately 20 μm in size, and less numerous in the AM100 compared to AF, (Fig. 1a, b). An SEM-EDX analysis of these RE particles showed that they were rich in Y, Al, and O, and contained also small amounts of Zr (Fig. 2a, d). The alloy produced with the AM process was almost fully dense, with only a small population of isolated pores in the submicron range.

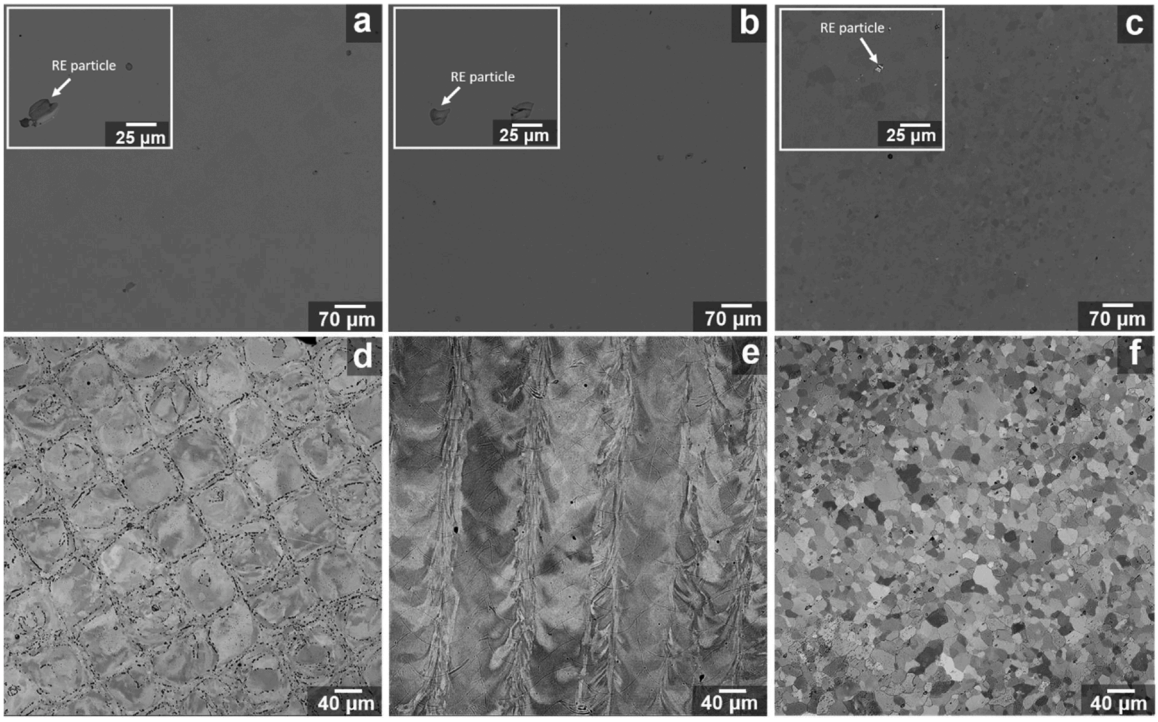

Fig. 1. SEM backscattered electron images of the samples prior to exposures: a, d) Polished and etched AM100-Z; b, e) Polished and etched AM100-Y; and c, f) Polished and etched AF.

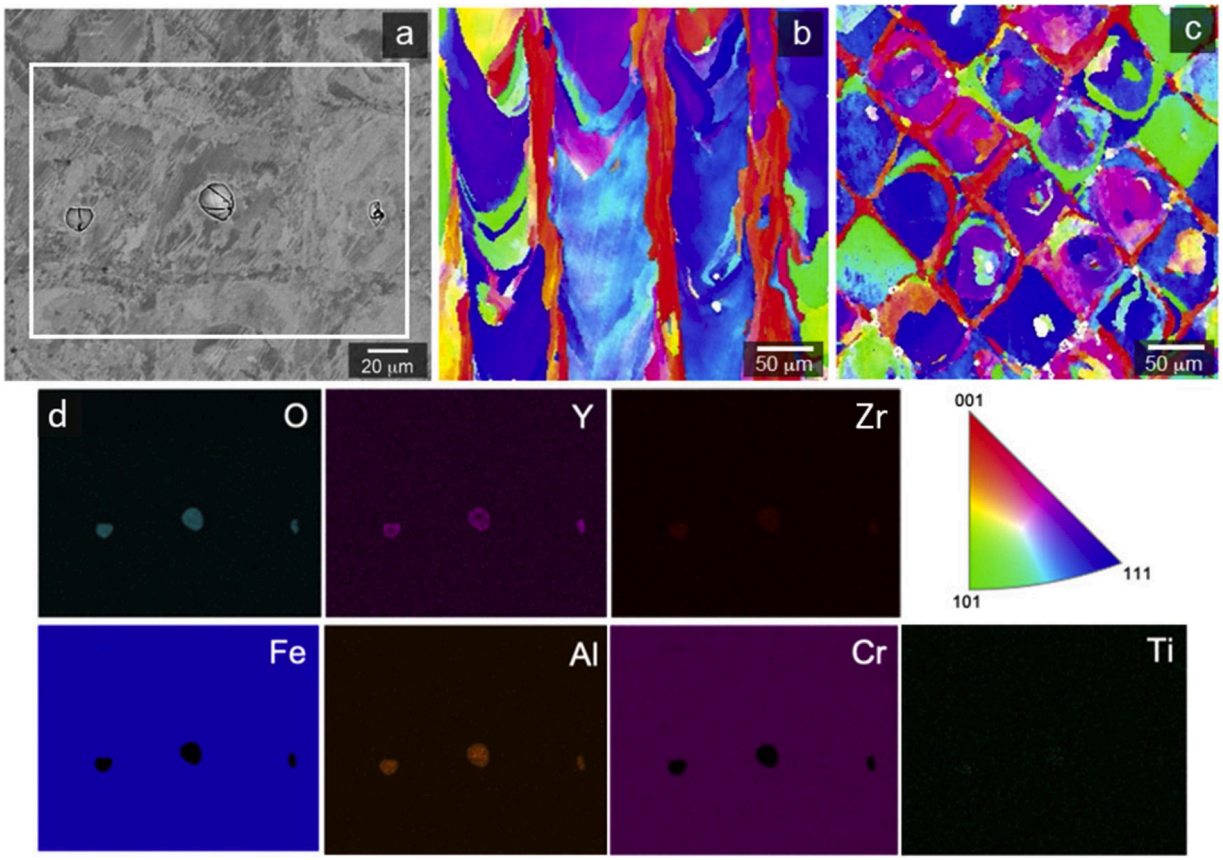

Fig. 2. SEM-EDX and EBSD IPF maps of AM-processed samples prior to exposures: a) SEM image AM100-Z; b) IPF map of AM100-Y; c) IPF map of AM100-Z; and d) EDX maps of the selected area shown in a).

3.2. Investigations after exposures

3.2.1. Oxidation kinetics

Fig. 3 shows the mass gain values of AF, AM100-Y, and AM100-Z after 168 h at 900 °C and 1100 °C. The recorded mass gains after the exposure at 900 °C, in particular, were very low, so that a meticulous handling of the samples was required to achieve a high degree of reproducibility. The mass gain values of AF matched well with earlier published data [12,38]. AM100-Y and AM100-Z exhibited approximately 15 % lower mass gain than AF exposed at 900 °C and 1100 °C. The reason for this difference could be related to the formation of the $MgAl_2O_4$ phase, as will be discussed in the microstructural investigations section. One of the important outcomes of the mass gain data is that AM100-Y and AM100-Z had almost the same mass gain

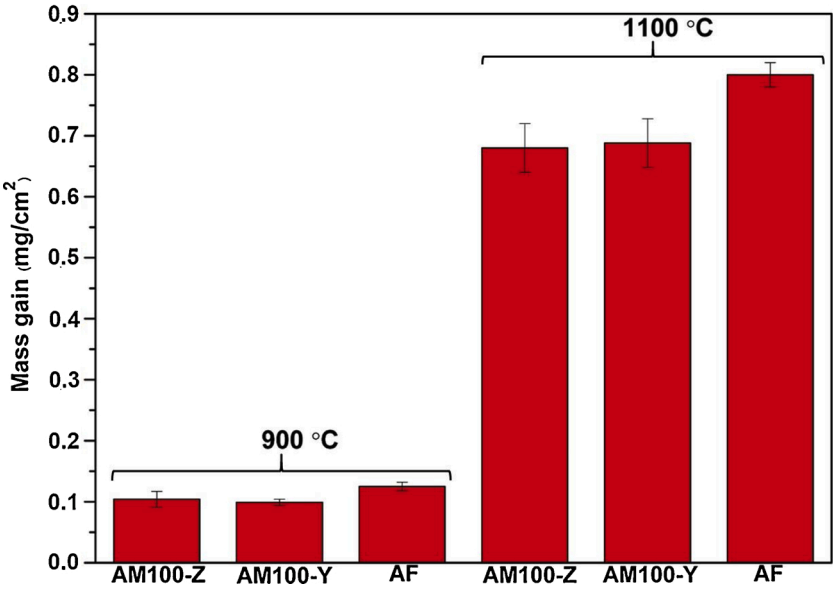

Fig. 3. Mass gains of AF, AM100-Y, and AM100-Z after 168 h at 900 °C and 1100 °C in dry air.

values at both 900 °C and 1100 °C, suggesting that the overall oxidation rate was not affected after 168 h by the differences in the orientation of the sample surface, i.e., perpendicular or parallel to the BD.

3.2.2. Phase analysis

The XRD diffractograms of oxidized AF and AM100-Z after 168 h at 900 °C and 1100 °C are presented in Fig. 4. The following phases were identified on AF after exposures at 900 °C and 1100 °C: $MgAl_2O_4$ (JCPDS file # 04−016-4047), α-Al_2O_3 (JCPDS file # 00−046-1212), and the alloy substrate (JCPDS file # 00−034-0396). α-Al_2O_3 and the alloy substrate were also visible on AM100-Z. The difference between the AF and AM100 alloys is that the TiO_2 (Rutile, JCPDS file # 04−003-0648) phase was observed on AM100-Z and $MgAl_2O_4$ was absent. This difference is probably related to a slight variation in trace element content between AM100 and AF (Table 1).

3.2.3. Microstructural investigations

Fig. 5 shows the plan-view SEM micrographs of oxidized AF, AM100-Y, and AM100-Z after 168 h at 900 °C and 1100 °C, and Fig. 6 shows the SEM-EDX elemental distribution on the surfaces of the same samples. Results from the cross-sectional analyses of the oxide scales formed on the investigated materials are presented in Figs. 7 and 8. They show the oxide scale microstructure and elemental distribution over the samples exposed at 1100 °C. Details on the oxide scale structures after the two exposures will be presented and discussed in this section.

The plan-view image of AF exposed at 900 °C (Fig. 5c) shows that the surface was covered with a uniform base oxide. The EDX analysis shows that the base oxide was rich in Al and Mg, confirming the XRD results. In addition to the base oxide, 2–10 μm-large RE particles, which appear bright in the back-scattered image, were found.

Similar to the AF material, a uniform base oxide was visible on both the AM100-Z (Fig. 5a) and AM100-Y (Fig. 5b) samples. Both samples also exhibited RE particles and some transient alumina nodules on their surfaces. Note in Fig. 5 that there is a difference in contrast between individual oxidized squares (Fig. 5a) and columns (Fig. 5b). Most of the narrow rims in Fig. 5a are also darker than the squares. SEM-EDX analysis showed that the darker rims are more enriched with Al and O at 900 °C (Fig. 6a, b) than the squares and columns. This difference in contrast and the enrichment of Al and O indicate a difference in oxide scale thickness and is discussed in the FIB and TEM-EDX sections below.

After exposure at 1100 °C, the oxide scale formed on AF was similar to the one formed at 900 °C, i.e., it consisted of a base oxide and oxidized RE particles. SEM-EDX analysis showed that the surface of the base oxide was rich in Al, Mg, and O.

The surface of AM100 was composed of a base oxide (α-Al_2O_3) on which small bright particles were uniformly distributed. The bright particles were identified as TiO_2 (rutile) according to XRD and SEM-EDX analyses (Figs. 4, 6). TiO_2 particles were coarser than at 900 °C, probably due to faster outward diffusion of Ti at higher temperatures. There was no image contrast on the surface between the large squares and columns at 1100 °C. However, the thicker oxide ridges on the narrow rims between the columns and squares remained visible for both AM100-Y and AM100-Z.

All specimens in the SEM cross-section images (Fig. 7) exhibited outward- and inward-growing double-layered oxide scales, separated by the original surface of the steel, typical for Al_2O_3-forming ferritic stainless steels [5,10,13]. The thickness ratio between these two oxide scales was approximately 1 at 900 °C for all specimens, while this ratio was 5–6 at 1100 °C. The higher ratio at 1100 °C was a result of the enhanced oxidation kinetics of RE-containing Fe-Cr-Al alloys. Hellstrom et al. [38] have reported similar behavior with the inner part of the scale becoming more dominant after longer exposure times on AF at 1100 °C. In addition to these findings, the cross-section images revealed that the concentration of pores in the outward-growing part of the oxide scale was much higher for AF than for AM100. The oxide scale was somewhat thicker for AF than for AM100, which is consistent with the mass gain data (Fig. 3), although there was substantial lateral variation in thickness. Fig. 7 clearly shows that the oxide scale was substantially thicker at 1100 °C than at 900 °C.

SEM-EDX elemental mapping was only performed on samples exposed at 1100 °C, as the spatial resolution was too poor to adequately analyze the thinner scales obtained at 900 °C. The EDX cross-section maps (Fig. 8) revealed that the outer scale of AF consisted of a Mg-rich band, while TiO_2 particles were found on the surface of AM100. A line scan (not given here) performed on AF revealed that the outer region where the Mg enrichment observed was composed of 9 at. % Mg, 32 at. % Al, and 59 at % O. The inner region was composed of 42 at. % Al and 58 at. % O. A line scan was performed on the outer scale of AM100-Z where a line coinciding with a Ti-rich particle was composed of 11 at. % Ti, 19 at. % Al, and 70 at. % O, and the inner region was composed of 41 at. % Al and 59 at. % O. The amount of Mg found on the Kanthal AF matched well with the XRD diffractograms ($MgAl_2O_4$) shown before in Fig. 4. However, the Ti content in the outer part of the oxide scale of AM100-Z was lower than the expected value when compared to XRD diffractograms (TiO_2). This was caused by the small size of the particle (around 600 nm) combined with the low spatial resolution of SEM, which resulted in a collection of Al signals near that region.

The occurrence of Mg-rich oxide on alumina has been observed before. Mayer et al. [39] have clearly shown that even small amounts of Mg (80 ppm) in Al_2O_3-forming stainless steels result in the formation

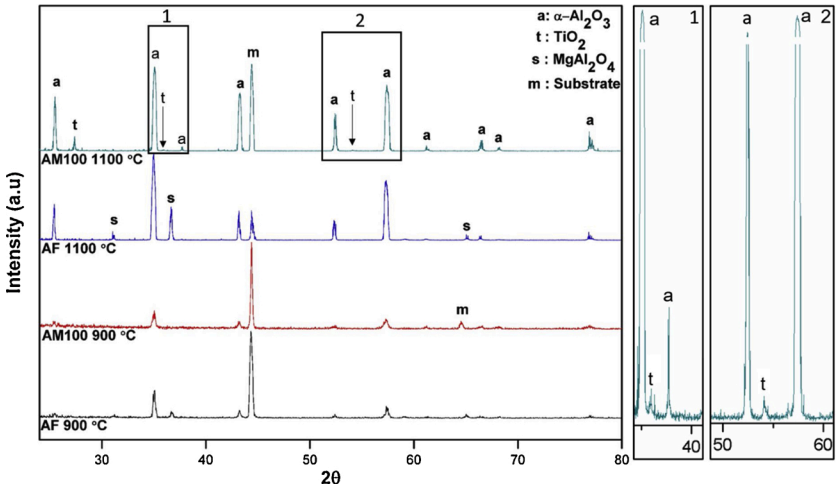

Fig. 4. XRD diffractogram of AF and AM100-Z sample after 168 h at 900 °C and 1100 °C in dry air.

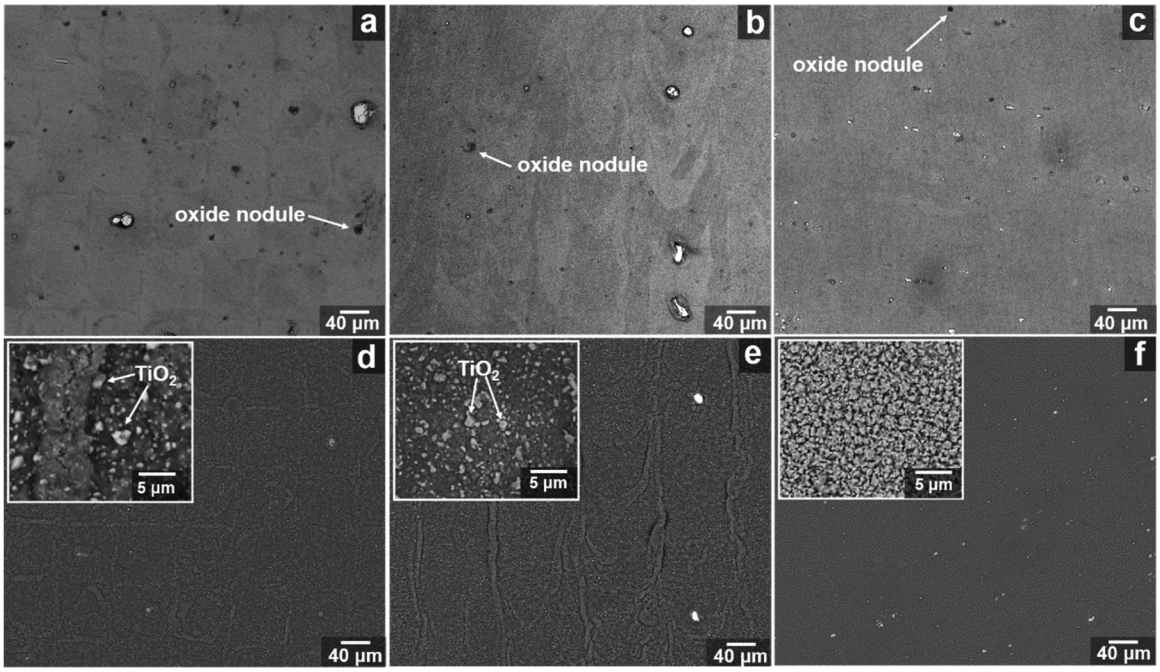

Fig. 5. SEM plan-view images of samples exposed at 900 °C for 168 h in dry air: a) AM100-Z; b) AM100-Y; and c) AF. SEM images after exposure to 1100 °C for 168 h: d) AM100-Z; e) AM100-Y; and f) AF.

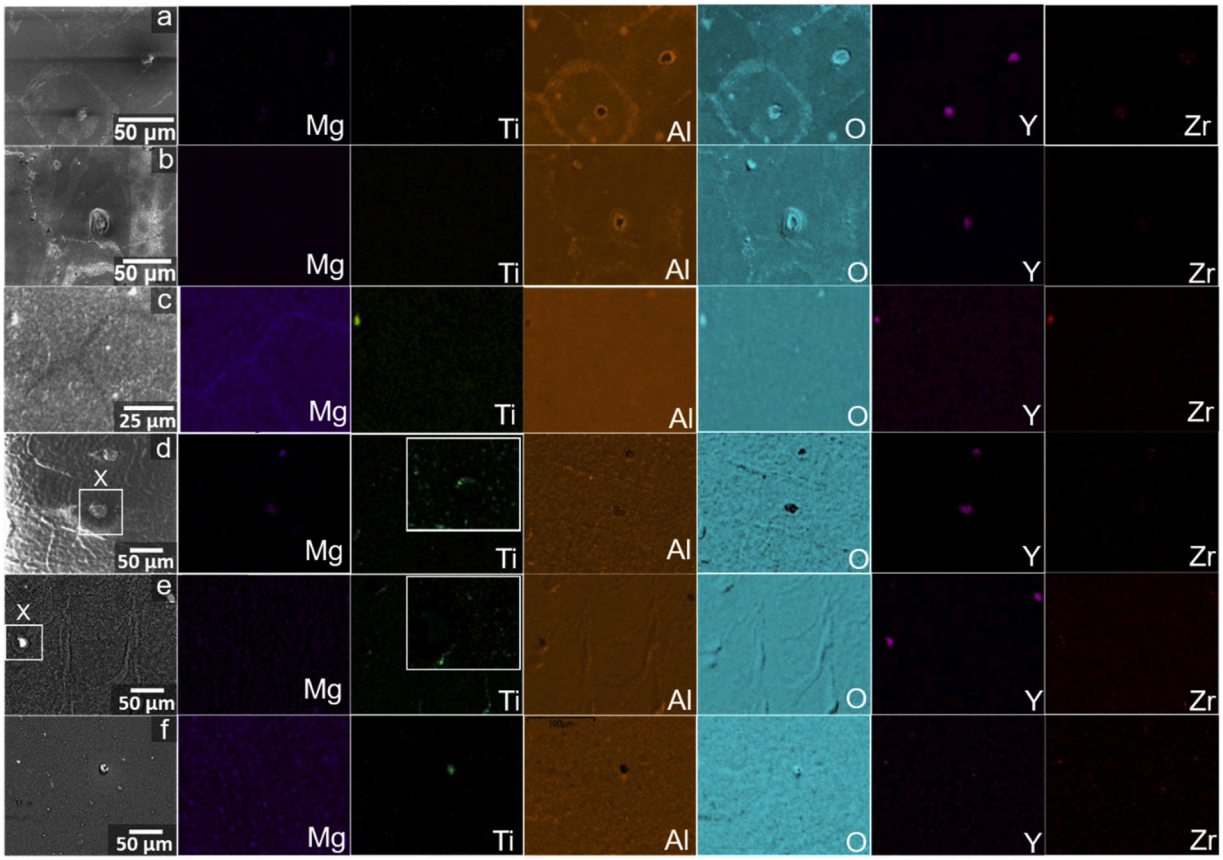

Fig. 6. Surface SEM secondary electron imaging and EDX analysis of samples exposed at 900 °C and 1100 °C for 168 h in dry air: a) AM100-Z; b) AM100-Y; and c) AF exposed at 900 °C. d) AM100-Z; e) AM100-Y; and f) AF exposed at 1100 °C.

$MgAl_2O_4$ on the surface of these steels. The formation of $MgAl_2O_4$ results in a change in volume, which causes the formation of the pores shown in Fig. 7c and f [39]. There are two possible mechanisms that might trigger the formation of the $MgAl_2O_4$ phase. The first mechanism relies on the formation of transient γ-Al_2O_3. In the early stages of oxidation, when the transient γ-Al_2O_3 phase is formed at the outermost layer of the scale, Mg

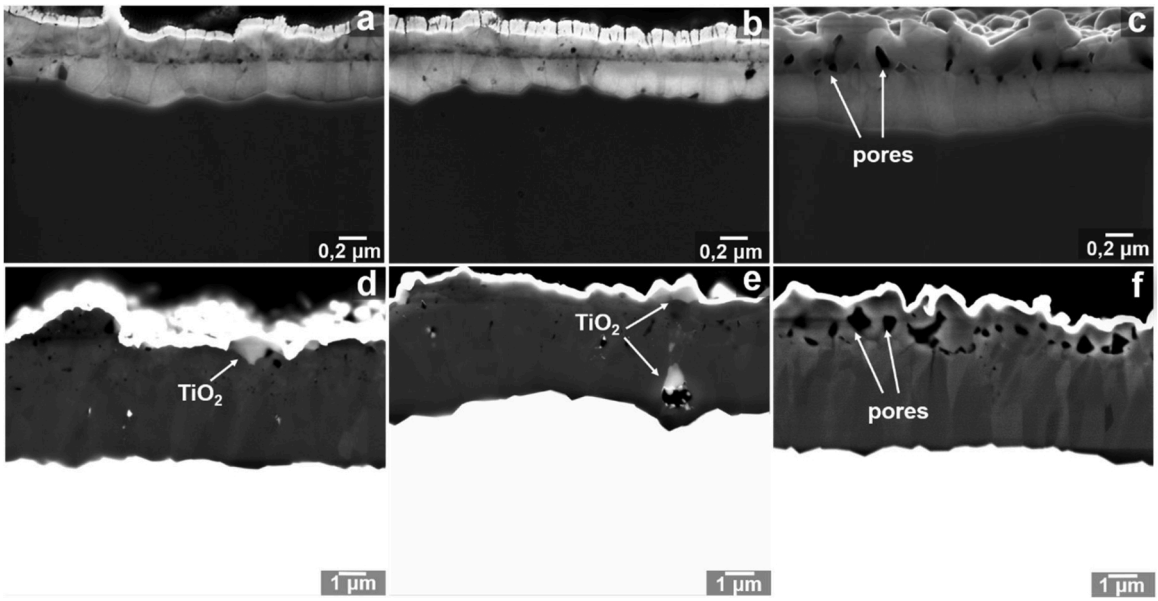

Fig. 7. SEM cross-section images of samples exposed at 900 °C and 1100 °C for 168 h in dry air: a) AM100-Z; b) AM100-Y; and c) AF exposed at 900 °C. d) AM100-Z; e) AM100-Y; and f) AF exposed at 1100 °C.

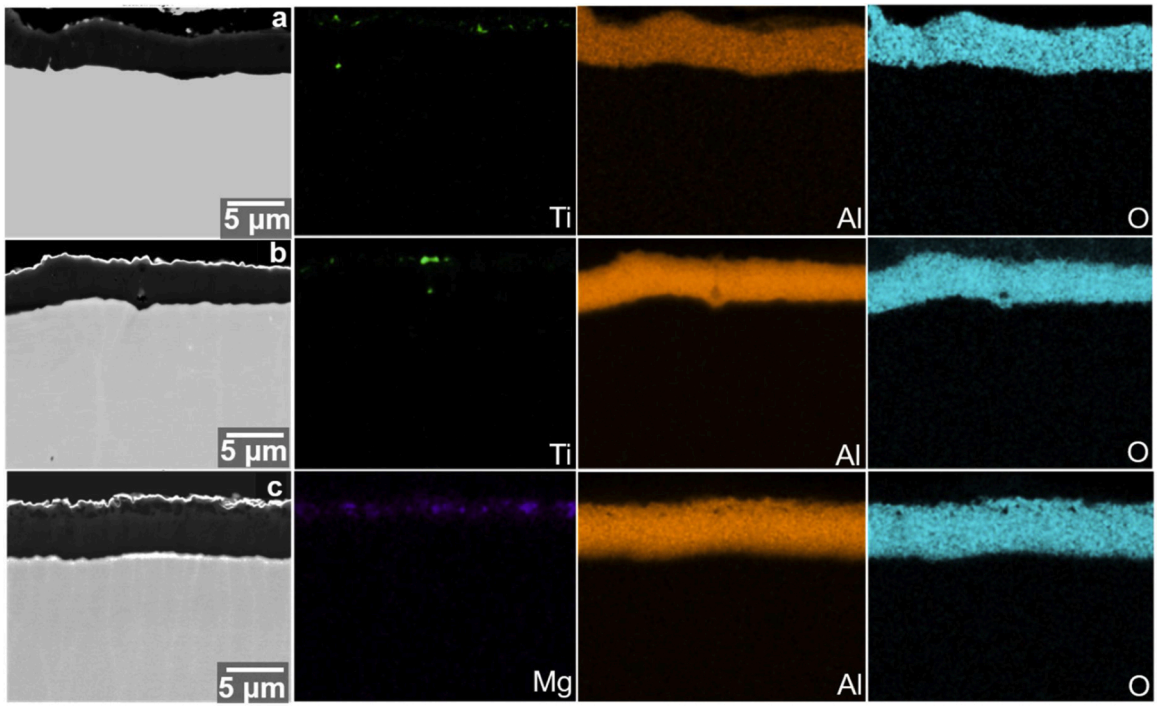

Fig. 8. Cross-sectional SEM-EDX analysis of samples exposed at 1100 °C for 168 h in dry air. a) AM100-Z, b) AM100-Y, C) AF.

is enriched in this layer due to its fast diffusion along the alloy grain boundaries and forms γ-$Al_{2-x}Mg_xO_{3-(x/2)}$. With time, the γ-$Al_{2-x}Mg_xO_{3-(x/2)}$ grains convert to a stable α-Al_2O_3 and $MgAl_2O_4$ spinel phase [13]. An alternative mechanism has been suggested by Mayer: Mg can diffuse through the grain boundaries of α-Al_2O_3 and react with it to form $MgAl_2O_4$ at the gas-oxide interface without relying on the formation of γ-Al_2O_3 [39]. The first mechanism is not valid at high temperatures (>1100 °C) since transient Al_2O_3 phases would immediately be converted into α-Al_2O_3. We believe that both mechanisms contribute to spinel formation in the present study, as the temperatures were lower (900 °C, 1100 °C) than in the study by Mayer (1200 °C).

Further in-depth microstructural characterization of the AM100 samples was carried out with scanning transmission electron microscopy (STEM) coupled with (EDX). Two site-specific cross-sectional samples were prepared using the FIB/SEM lift-out technique: one from AM100-Z 900 °C and the other from AM100-Z 1100 °C (see areas marked in Figs. 9 and 10).

Thin (500 nm on average) and thick (900 nm on average) parts of the oxide scale were distinguishable in the STEM high angle annular dark field (HAADF) micrograph taken from the AM100-Z 900 °C sample (Fig. 9b). The thicker part of the scale also appears in the figure to have a more undulating surface. The thickness of the oxide scale contained on the rims between the two squares is comparable to thickness of the oxide scale on the right square in Fig. 9, at least for the scale close to the rim. A

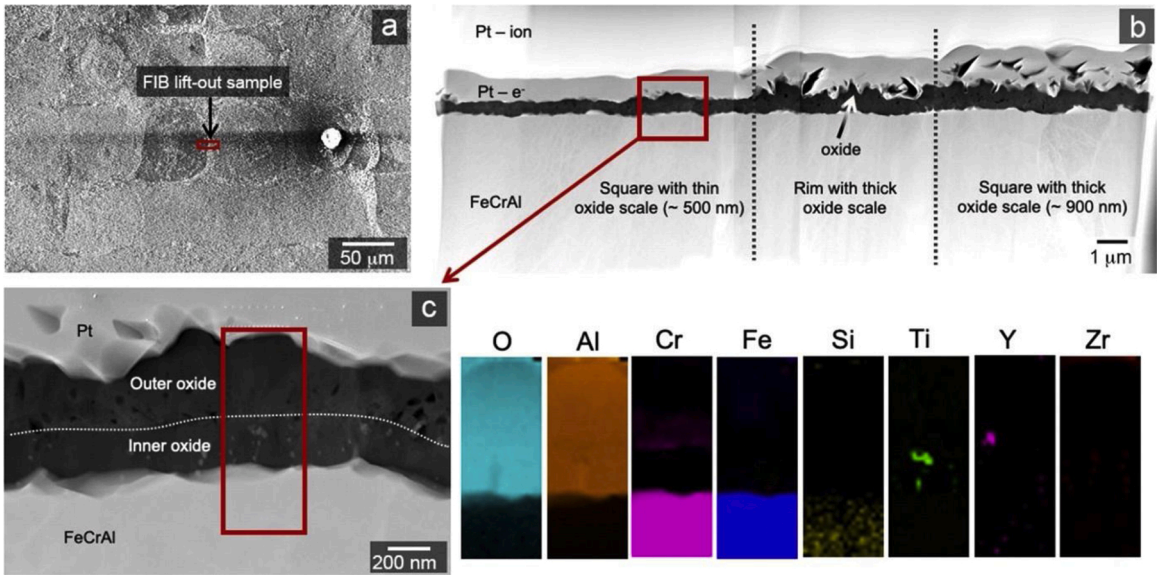

Fig. 9. FIB lift-out and cross-sectional STEM-EDX analysis of the AM100-Z sample exposed at 900 °C for 168 h. a) FIB lift-out region. b) STEM HAADF micrograph showing the oxide scale grown on two squares separated by a rim. c) Higher magnification STEM HAADF micrograph with corresponding EDX maps from the boxed region.

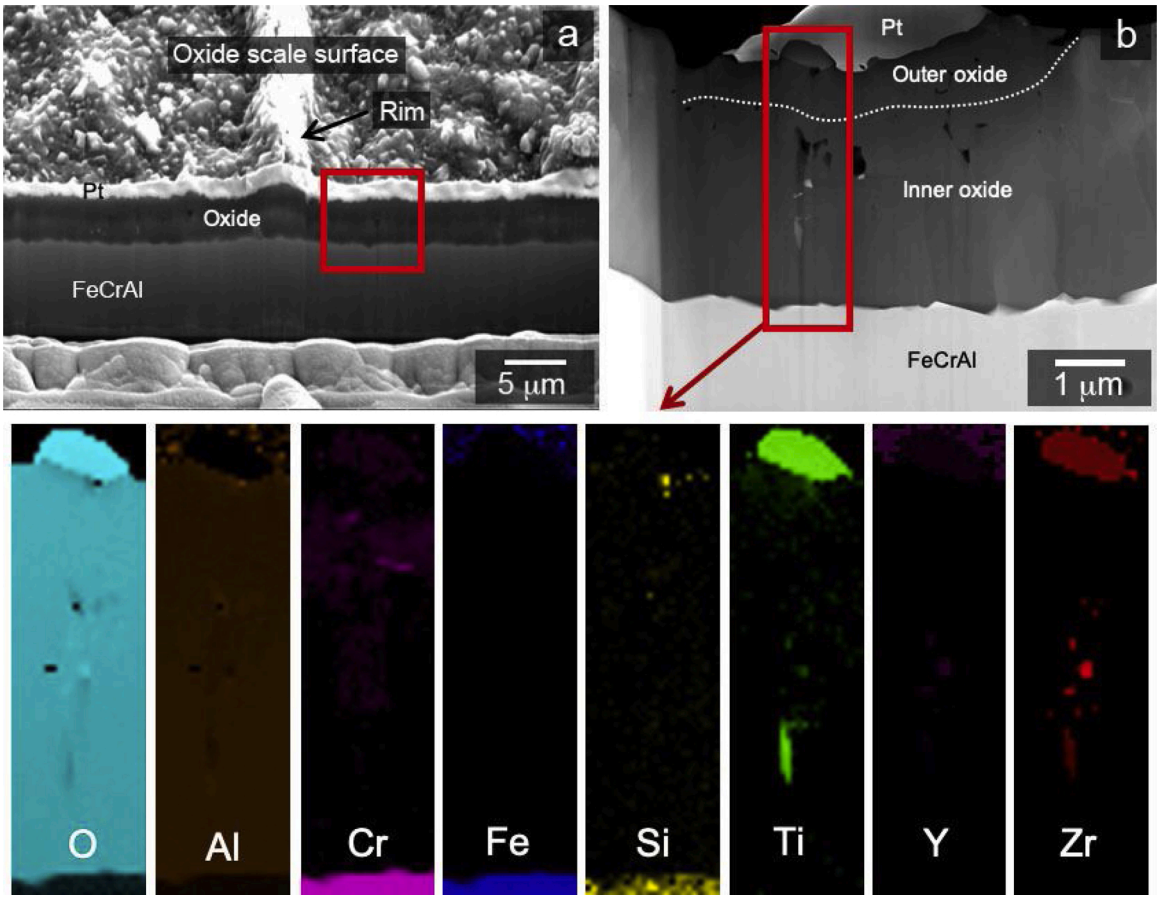

Fig. 10. FIB lift-out and cross-sectional STEM-EDX analysis of the AM100-Z sample exposed at 1100 °C for 168 h. A) FIB lift-out region. b) STEM HAADF cross-section micrograph. EDX analysis (boxed region) of the oxide scale formed on the right square in a).

closer look at the thinner oxide scale at higher magnification (Fig. 9c) revealed a porous outward-growing oxide and a fairly dense inward-growing oxide. A Cr-enriched band at the boundary between the inner and the outer part of the oxide scale can be seen in the EDX Cr map (Fig. 9c). Some heavy-element-containing particles (bright particles in the HAADF micrograph, Fig. 9c) dispersed mostly in the inward-growing oxide scale were visible. EDX elemental mapping showed that these bright particles mainly contained Ti and Zr. An isolated Y-rich RE

particle was also found in the outward-growing oxide scale. The RE particles in the oxide scale were most likely oxidized, however, it is not possible to confirm this with EDX due to the presence of the oxygen X-ray signal from the surrounding oxide scale. The Ti EDX map in Fig. 9 shows the presence of Ti in the inner part of the oxide scale, indicating that Ti diffused through the grain boundaries of the oxide to the surface-forming TiO_2 phase on the surface, as confirmed with XRD (Fig. 4) and seen in the SEM-EDX data (Figs. 7e, 8b). Similar results have been reported in the literature [40,41]. Ti is not soluble in the alumina scale, and TiO_2 is less stable than α-Al_2O_3 [42,43]. Therefore, during the oxidation, Ti rapidly diffused through the grain boundaries, was enriched at the gas-oxide interface, and formed TiO_2 particles owing to the high oxygen affinity and small cation size of Ti [44–47].

The AM100-Z 1100 °C sample did not show any distinct variation in the thickness of the oxide scale among the different squares. However, the oxide scale formed on the narrow rims between the squares was noticeably thicker (Fig. 10a). These results obtained with detailed microscopy clearly show that, at 900 °C, the contrast difference between individual squares/columns, and between narrow rims and squares in the plan view images (Fig. 5a, b) occurred because of the formation of thin and thick oxide scales. More backscattered electrons were generated from the underlying metal of the thinner section of the oxide scales, so these areas appear brighter in the image. As mentioned in investigation of alloys prior to exposure, the IPF maps (Fig. 2) revealed that there exists a variation in orientation from grain to grain, which could cause the differences in oxide scale thickness by affecting the oxide grain size and short circuit diffusion paths, as shown by Tyagi et al. [48]. However, our results obtained at 1100 °C show that the only noticeable difference in thickness was between the oxide scale formed on the rims and the oxide scale formed on squares and/or columns. Thus, due to the enhanced kinetics at 1100 °C and after 168 h, the effect of the differences in orientation on oxide scale thickness was negligible. Therefore, the oxide scale formed on the rims was thicker probably because of the fine-grained nature of the alloy on the rims at both 900 °C and 1100 °C. The mechanism of the formation of thin and thick oxide scales on AM100 will be investigated in subsequent work.

The STEM HAADF micrograph in Fig. 10b shows the typical oxide scale morphology for inward- and outward-growing oxides with a thick scale (about 3.7 μm) and high inward-to-outward ratio. This was the result of faster kinetics at the higher temperature, as noted in Fig. 7. The outer part of oxide layer was composed of equiaxed grains, while the inner part consisted of coarser columnar grains. This is typically found in the literature on RE-containing Fe-Cr-Al alloys [13,38,49–51]. TEM-EDX elemental mapping showed a Cr-enriched band at the boundary between inward- and outward-growing oxide scales, which corresponds to the original surface of the steel. Similar to the AM100-Z 900 °C sample, Ti and Zr were joined in the form of small RE particles within the inner oxide layer. An oxidized, relatively large (<1 μm) RE particle rich in Ti and Zr was visible at the gas-oxide interface.

4. Conclusions

This study investigated the effect of additive manufacturing on the oxidation properties of RE-containing FeCrAl alloys. The oxidation properties of surfaces parallel (Y cut) and perpendicular (Z cut) to the BD at 900 °C and 1100 °C were compared with conventionally manufactured AF. The mass gain values did not show any substantial difference between exposed Y and Z cut, but the AM materials exhibited slightly lower mass gains than the conventionally produced material. It is suggested that this difference is due to a slight variation in the chemical composition of the materials used. The analysis of the oxide scales revealed a variation in scale thickness. The variation correlates with the underlying metal microstructure. It is suggested that the difference in thickness found among the different squares after exposure at 900 °C is because the underlying metal grains have a difference in orientation. This contrast was absent at 1100 °C because of the larger overall thickness of the oxide. There was also a difference in thickness among the scales formed on the narrow rims and the squares. This is probably because of the fine-grained nature of the underlying metal in these regions; this difference was also apparent after exposure at 1100 °C. The AM-processed FeCrAl material behaved very similar to the conventionally produced AF. Although some local differences in oxidation rate were observed, these seemed to stem mostly from the initial stage of the formation of an oxide scale and would probably have no effect on the overall oxidation kinetics and lifetime of a component over its service life. However, further tests for longer durations and cycles should be conducted for a more detailed investigation into the lifetime of AM components.

Data availability

The raw/processed data required to reproduce these findings will be made available upon request.

CRediT authorship contribution statement

K. Ozgur Gunduz: Conceptualization, Investigation, Writing - original draft, Writing - review & editing. **Alberto Visibile:** Investigation, Writing - review & editing. **Mohammad Sattari:** Investigation, Validation, Writing - review & editing. **Irina Fedorova:** Investigation, Validation. **Saud Saleem:** Conceptualization, Investigation, Resources, Writing - review & editing. **Krystyna Stiller:** Validation, Writing - review & editing. **Mats Halvarsson:** Conceptualization, Funding acquisition, Project administration, Supervision, Writing - review & editing. **Jan Froitzheim:** Conceptualization, Funding acquisition, Project administration, Supervision, Writing - review & editing.

Declaration of Competing Interest

The authors declare that they have no known competing financial interests or personal relationships that could have appeared to influence the work reported in this paper.

Acknowledgements

This work was carried out at the Swedish High Temperature Corrosion Centre (HTC) at Chalmers University of Technology and is hereby gratefully acknowledged together with the Swedish Energy Agency and its member companies (AB Sandvik Materials Technology, Kanthal AB, Siemens Energy AB). This work was also performed in part at the Chalmers Materials Analysis Laboratory, CMAL.

References

[1] W.J. Ding, H. Shi, A. Jianu, Y.L. Xiu, A. Bonk, A. Weisenburger, T. Bauer, Molten chloride salts for next generation concentrated solar power plants: mitigation strategies against corrosion of structural materials, Sol. Energy Mater. Sol. Cells 193 (2019) 298–313.
[2] J. Engkvist, S. Canovic, F. Liu, H. Gotlind, J.E. Svensson, L.G. Johansson, M. Olsson, M. Halvarsson, Oxidation of FeCrAl foils at 500-900 degrees C in dry O-2 and O-2 with 40% H2O, Mater. High Temp. 26 (2009) 199–210.
[3] J.K. Bunn, R.L. Fang, M.R. Albing, A. Mehta, M.J. Kramer, M.F. Besser, J. R. Hattrick-Simpers, A high-throughput investigation of Fe-Cr-Al as a novel high-temperature coating for nuclear cladding materials, Nanotechnology 26 (2015).
[4] B.A. Pint, K.A. Terrani, M.P. Brady, T. Cheng, J.R. Keiser, High temperature oxidation of fuel cladding candidate materials in steam-hydrogen environments, J. Nucl. Phys. Mater. Sci. Radiat. Appl. 440 (2013) 420–427.
[5] W.J. Quadakkers, D. Naumenko, E. Wessel, K.V.L. Singheiser, Growth rates of alumina scales on Fe-Cr-Al alloys, Oxid. Met. 61 (2004) 17–37.
[6] J.R. Nicholls, M.J. Bennett, R. Newton, A life prediction model for the chemical failure of FeCrAlRE alloys: preliminary assessment of model extension to lower temperatures, Mater. High Temp. 20 (2003) 429–438.
[7] D.J. Prior, H. Al-Badairy, G.G.E. Seward, C.J. Veltkamp, G.J. Tatlock, Microstructural development of alpha alumina scales developed on FeCrAl alloys, Mater. Sci. Tech. Lond. 22 (2006) 1316–1324.
[8] S. Canovic, J. Engkvist, F. Liu, H. Lai, H. Gotlind, K. Hellstrom, J.E. Svensson, L. G. Johansson, M. Olsson, M. Halvarsson, Microstructural investigation of the initial

oxidation of the FeCrAlRE alloy kanthal AF in dry and wet O-2 at 600 and 800 degrees C, J. Electrochem. Soc. 157 (2010) C223–C230.
[9] J. Jedlinski, G. Borchardt, On the oxidation mechanism of alumina formers, Oxid. Met. 36 (1991) 317–337.
[10] S. Yoneda, S. Hayashi, S. Ukai, The transition from transient oxide to protective Al2O3 scale on Fe-Cr-Al alloys during heating to 1000 a degrees C, Oxid. Met. 89 (2018) 81–97.
[11] G. Berthome, E. N'Dah, Y. Wouters, A. Galerie, Temperature dependence of metastable alumina formation during thermal oxidation of FeCrAl foils, Mater. Corros. 56 (2005) 389–392.
[12] H. Josefsson, F. Liu, J.E. Svensson, M. Halvarsson, L.G. Johansson, Oxidation of FeCrAl alloys at 500-900 degrees C in dry O-2, Mater. Corros. 56 (2005) 801–805.
[13] H. Gotlind, F. Liu, J.E. Svensson, M. Halvarsson, L.G. Johansson, The effect of water vapor on the initial stages of oxidation of the FeCrAl alloy Kanthal AF at 900 degrees C, Oxid. Met. 67 (2007) 251–266.
[14] F. Liu, H. Gotlind, J.E. Svensson, L.G. Johansson, M. Halvarsson, Early stages of the oxidation of a FeCrAlRE alloy (Kanthal AF) at 900 degrees C: a detailed microstructural investigation, Corros. Sci. 50 (2008) 2272–2281.
[15] R. Cueff, H. Buscail, E. Caudron, C. Issartel, F. Riffard, Influence of yttrium-alloying addition on the oxidation of alumina formers at 1173 K, Oxid Met 58 (2002) 439–455.
[16] F.H. Stott, G.C. Wood, F.A. Golightly, The isothermal oxidation behaviour of Fe-Cr-Al and Fe-Cr-Al-Y alloys at 1200°C, Corros. Sci. 19 (1979) 869–887.
[17] R. Cueff, H. Buscail, E. Caudron, C. Issartel, F. Riffard, Oxidation behaviour of Kanthal A1 and Kanthal AF at 1173 K: effect of yttriurn alloying addition, Appl. Surf. Sci. 207 (2003) 246–254.
[18] M.J. Bennett, R. Newton, J.R. Nicholls, H. Al-Badairy, G.J. Tatlock, The Oxidation Behaviour of the Commercial FeCrAIRE Alloys Aluchrom YHf and Kanthal AF Foils in Air at 800 Degrees-950 Degrees C, High Temperature Corrosion and Protection of Materials 6, Prt 1 and 2, Proceedings, 461-464, 2004, pp. 463–472.
[19] B.A. Pint, S. Dryepondt, K.A. Unocic, D.T. Hoelzer, Development of ODS FeCrAl for compatibility in fusion and fission energy applications, JomUs 66 (2014) 2458–2466.
[20] B. Jonsson, Q. Lu, D. Chandrasekaran, R. Berglund, F. Rave, Oxidation and creep limited lifetime of kanthal APMT(A (R)), a dispersion strengthened FeCrAlMo alloy designed for strength and oxidation resistance at high temperatures, Oxid Met 79 (2013) 29–39.
[21] S. Chevalier, Formation and Growth of Protective Alumina Scales, 2008, pp. 290–328.
[22] N. Pugacheva, E. Ekzemplyarova, S. Zadvorkin, Effect of aluminium on the structure and physical properties of Fe-Cr-Al alloys, Russ. Metall. 2006 (2006) 61–68.
[23] T. DebRoy, H.L. Wei, J.S. Zuback, T. Mukherjee, J.W. Elmer, J.O. Milewski, A. M. Beese, A. Wilson-Heid, A. De, W. Zhang, Additive manufacturing of metallic components - process, structure and properties, Prog. Mater. Sci. 92 (2018) 112–224.
[24] W.E. Frazier, Metal additive manufacturing: a review, J. Mater. Eng. Perform. 23 (2014) 1917–1928.
[25] A. Sola, A. Nouri, Microstructural porosity in additive manufacturing: the formation and detection of pores in metal parts fabricated by powder bed fusion, J. Adv. Manuf. Process. (2019).
[26] Y. Kok, X.P. Tan, P. Wang, M.L.S. Nai, N.H. Loh, E. Liu, S.B. Tor, Anisotropy and heterogeneity of microstructure and mechanical properties in metal additive manufacturing: a critical review, Mater Design 139 (2018) 565–586.
[27] M. Ni, C. Chen, X.J. Wang, P.W. Wang, R.D. Li, X.Y. Zhang, K.C. Zhou, Anisotropic tensile behavior of in situ precipitation strengthened Inconel 718 fabricated by additive manufacturing, Mat. Sci. Eng. a-Struct. 701 (2017) 344–351.
[28] L. Hitzler, J. Hirsch, B. Heine, M. Merkel, W. Hall, A. Ochsner, On the anisotropic mechanical properties of selective laser-melted stainless steel, Materials 10 (2017).
[29] H. Kyogoku, T.T. Ikeshoji, A review of metal additive manufacturing technologies: mechanism of defects formation and simulation of melting and solidification phenomena in laser powder bed fusion process, Mech. Eng. Rev 7 (2020).
[30] W.J. Sames, F.A. List, S. Pannala, R.R. Dehoff, S.S. Babu, The metallurgy and processing science of metal additive manufacturing, Int. Mater. Rev. 61 (2016) 315–360.
[31] Y.N. Shi, Z. Lu, L. Yu, R. Xie, Y.H. Ren, G. Yang, Microstructure and tensile properties of Zr-containing ODS-FeCrAl alloy fabricated by laser additive manufacturing, Mat. Sci. Eng. a Struct. 774 (2020).
[32] F. Liu, H. Gotlind, J.E. Svensson, L.G. Johansson, M. Halvarsson, TEM investigation of the microstructure of the scale formed on a FeCrAlRE alloy at 900 a degrees C: the effect of Y-rich RE particles, Oxid Met 74 (2010) 11–32.
[33] A. Zinoviev, O. Zinovieva, V. Ploshikhin, V. Romanova, R. Balokhonov, Evolution of grain structure during laser additive manufacturing. Simulation by a cellular automata method, Mater Design 106 (2016) 321–329.
[34] T. Wang, Y.Y. Zhu, S.Q. Zhang, H.B. Tang, H.M. Wang, Grain morphology evolution behavior of titanium alloy components during laser melting deposition additive manufacturing, J. Alloys. Compd. 632 (2015) 505–513.
[35] M.S. Pham, B. Dovgyy, P.A. Hooper, Twinning induced plasticity in austenitic stainless steel 316L made by additive manufacturing, Mat. Sci. Eng. a-Struct. 704 (2017) 102–111.
[36] K. Antony, N. Arivazhagan, Studies on energy penetration and marangoni effect during laser melting process, J. Eng. Sci. Technol 10 (2015) 509–525.
[37] T. Mukherjee, W. Zhang, T. DebRoy, An improved prediction of residual stresses and distortion in additive manufacturing, Comp. Mater. Sci. 126 (2017) 360–372.
[38] K. Hellstrom, N. Israelsson, N. Mortazavi, S. Canovic, M. Halvarsson, J.E. Svensson, L.G. Johansson, Oxidation of a dispersion-strengthened powder metallurgical FeCrAl alloy in the presence of O-2 at 1,100 a degrees C: the influence of water vapour, Oxid. Met. 83 (2015) 533–558.
[39] J. Mayer, H.J. Penkalla, A. Dimyati, M. Dani, R. Untoro, D. Naurnenko, W. J. Quadakkers, Time dependence of Mg-incorporation in alumina scales on FeCrAl alloys studied by FIB-prepared TEM cross sections, Mater. High Temp. 20 (2003) 413–419.
[40] K.A. Unocic, E. Essuman, S. Dryepondt, B.A. Pint, Effect of environment on the scale formed on oxide dispersion strengthened FeCrAl at 1050°C and 1100°C, Mater. High Temp. 29 (2012) 171–180.
[41] B.A. Pint, Progress in understanding the reactive element effect since the whittle and stringer literature review, Proc. John Stringer Symposium on High Temperature Corrosion (2001) 9–19.
[42] A.H. Heuer, T. Nakagawa, M.Z. Azar, P.B. Hovis, J.L. Smialek, B. Gleeson, N.D. M. Hine, H. Guhl, H.S. Lee, P. Tangney, W.M.C. Foulkes, M.W. Finnis, On the growth of Al2O3 scales, Acta Mater. 61 (2013) 6670–6683.
[43] T. Boll, K.A. Unocic, B.A. Pint, K. Stiller, Interfaces in oxides formed on NiAlCr doped with Y, Hf, Ti, and B, Microsc. Microanal. 23 (2017) 396–403.
[44] B.A. Pint, K.B. Alexander, Grain boundary segregation of cation dopants in alpha-A (2)O(3) scales, J. Electrochem. Soc. 145 (1998) 1819–1829.
[45] B.A. Pint, K.A. Unocic, Ionic segregation on grain boundaries in thermally grown alumina scales, Mater High Temp 29 (2012) 257–263.
[46] B.A. Pint, A.J. Garratt-Reed, L.W. Hobbs, Possible role of the oxygen potential gradient in enhancing diffusion of foreign ions on alpha-Al2O3 grain boundaries, J. Am. Ceram. Soc. 81 (1998) 305–314.
[47] W.J. Quadakkers, D. Naumenko, L. Singheiser, H.J. Penkalla, A.K. Tyagi, A. Czyrska-Filemonowicz, Batch to batch variations in the oxidation behaviour of alumina forming Fe-based alloys, Mater Corros 51 (2000) 350–357.
[48] A.K. Tyagi, K. Szot, A. Czyrska-Filemonowicz, D. Naumenko, W.J. Quadakkers, Significance of crystallographic grain orientation for oxide scale formation on FeCrAlODS alloys studied by AFM and MCs+-SIMS, Mater. High Temp. 17 (2000) 159–163.
[49] J.A. Nychka, D.R. Clarke, Quantification of aluminum outward diffusion during oxidation of FeCrAl alloys, Oxid. Met. 63 (2005) 325–352.
[50] D.J. Young, D. Naumenko, L. Niewolak, E. Wessel, L. Singheiser, W.J. Quadakkers, Oxidation kinetics of Y-doped FeCrAl-alloys in low and high pO(2) gases, Mater. Corros. 61 (2010) 838–844.
[51] T.H. Huang, D. Naumenko, P. Song, J.S. Lu, W.J. Quadakkers, Effect of titanium addition on alumina growth mechanism on yttria-containing FeCrAl-Base alloy, Oxid. Met. 90 (2018) 671–690.